PNAS RESEARCH ARTICLE | BIOCHEMISTRY

Structural insights into RNA recognition by the *Staphylococcus aureus* exoribonuclease YhaM

Jacob M. Mattingly[a,b,1], Anna Lipońska[c,1], Julia Tanquary[a,b,1], Mee-Ngan F. Yap[c,2], and Christine M. Dunham[a,d,2]

Edited by Gisela Storz, National Institute of Child Health and Human Development, Bethesda, MD; received January 1, 2026; accepted May 8, 2026

Bacterial ribonucleases regulate gene expression in response to environmental stress and host interactions. In *Staphylococcus aureus,* the hibernation-promoting factor (Hpf) induces the formation of RNase R-resistant 100S ribosomes. We previously showed that the 3'-5' exoribonuclease YhaM cleaves the *hpf* transcript, reducing Hpf synthesis and leading to ribosome degradation. No structure of any YhaM homolog bound to RNA is available, and biological investigations of YhaM remain limited. Here, we find that deletion of *yhaM* attenuates *S. aureus* virulence in a *Galleria mellonella* infection model. We further determined electron cryomicroscopy structures of YhaM–RNA complexes. YhaM adopts a hexameric complex arranged in a ring, with its N-terminal oligonucleotide/oligosaccharide-binding (OB) domains positioned on both sides of the ring while the catalytic histidine/aspartate-rich (HD) domain active sites are buried within the interior. The OB-1" domains recognize the *hpf* hairpin by the formation of complementary minor groove interactions. RNA binding by two YhaM OB domains is mediated through engagement of both the backbones and nucleobases of the RNA substrate, where stacking of aromatic residues and nucleobases likely contributes to substrate recognition. Structures of YhaM bound to a single-stranded RNA reveal how the 3' ends of two RNAs are positioned within the HD domain poised for catalysis. Although six YhaM active sites are present, only two engage in RNA cleavage and further point to the importance of the remaining YhaM monomers as structural scaffolds for guiding RNA to the active site. In summary, these findings provide insights into the unique assembly of an understudied bacterial RNase.

ribonucleases | *Staphylococcus aureus* | protein synthesis | hibernation

Significance

Ribonucleases are essential for RNA processing, decay, and nucleotide recycling across all domains of life. This study sheds light on the atypical structural assembly of RNA-bound *Staphylococcus aureus* YhaM and how its oligonucleotide/oligosaccharide-binding (OB) domains engage both ssRNA and its endogenous target, the 3'-end hairpin of the *hpf* messenger RNA (mRNA). YhaM is required for macrophage invasion and full virulence in an insect model of bacteremia. This work highlights how YhaM engages the *hpf* mRNA, whose gene product is critical for ribosome stabilization and translational regulation.

Ribosome hibernation is a universal survival strategy adapted to prevent translation and preserve ribosome integrity during stress conditions (1–7). In the opportunistic human pathogen *Staphylococcus aureus*, the hibernation-promoting factor (Hpf) induces the dimerization of 70S ribosomes to form a translationally silent 100S complex (8–10). Perturbing the biogenesis and disassembly of 100S ribosomes significantly impairs *S. aureus* colonization in a murine model of bacteremia (11–13). Ribosomes lacking Hpf are prone to degradation by the exoribonuclease RNase R, which shares overlapping binding sites with Hpf (8, 14, 15). We previously showed that a poorly characterized 3'-5' exonuclease, YhaM (formerly Cbf1), trims the 3'-end of the *hpf* mRNA harboring an intrinsic terminator, leading to destabilization of the transcript and a reduction in 100S ribosome formation (16). Despite its broad conservation in Gram-positive bacteria and archaea (17), the native RNA targets of YhaM have only recently begun to emerge.

Because YhaM can bind to both DNA and RNA, its cellular role may be species- and/or condition-dependent. For example, YhaM from *S. aureus*, *Staphylococcus epidermidis*, and *Bacillus subtilis* cleaves both single-stranded (ss)DNA and ssRNA in vitro and has been implicated in DNA replication (18–22). In *B. subtilis,* YhaM was identified as a putative binding partner of the DnaC helicase in a yeast-two-hybrid screen (22), however, this interaction and its functional significance have not been rigorously validated. Moreover, *B. subtilis* YhaM does not appear to participate in the DNA damage response (20). In *S. epidermidis*, where *yhaM* is essential (23), YhaM processes CRISPR RNAs from the Type III-A CRISPR-Cas10-Csm system in vitro, and its activity is blocked by Csm5 (19). Despite these advances, the precise role of YhaM homologs in RNA turnover remains incompletely defined. In *B. subtilis* and *Streptococcus pyogenes*, YhaM exhibits low processivity in vivo, trimming only 1-6 nucleotides from mRNAs that are enriched in 3'-poly-U sequences and contain intrinsic terminators (24–26). In contrast, *Streptococcus pneumoniae* YhaM stabilizes sRNAs following 3' trimming rather than degrading them (27). YhaM also differentially regulates natural competence, promoting DNA uptake in *B. subtilis* but suppressing this process in *S. pneumoniae* (20, 27). *S. aureus* is not naturally competent for genetic transformation, suggesting that *S. aureus* YhaM serves a role distinct from

Author affiliations: [a]Department of Chemistry, Emory University, Atlanta, GA 30322; [b]Graduate Program in Biochemistry, Cell and Developmental Biology, Graduate Division of Biological and Biomedical Sciences, Emory University, Atlanta, GA 30322; [c]Department of Microbiology-Immunology, Northwestern University Feinberg School of Medicine, Chicago, IL 60611; and [d]Emory Antibiotic Resistance Center, Emory University, Atlanta, GA 30322

Author contributions: J.M.M., A.L., J.T., M.-N.F.Y., and C.M.D. designed research; J.M.M., A.L., and J.T. performed research; J.M.M., A.L., M.-N.F.Y., and C.M.D. analyzed data; and J.M.M., A.L., J.T., M.-N.F.Y., and C.M.D. wrote the paper.

The authors declare no competing interest.

This article is a PNAS Direct Submission.

[1]J.M.M., A.L., and J.T. contributed equally to this work.

[2]To whom correspondence may be addressed. Email: frances.yap@northwestern.edu or christine.m.dunham@emory.edu.

This article contains supporting information online at https://www.pnas.org/lookup/suppl/doi:10.1073/pnas.2600028123/-/DCSupplemental.

Published June 16, 2026.

competence regulation. Collectively, these phenotypic differences indicate that YhaM homologs likely have species-specific functions. Given that YhaM affects the stability of hundreds of transcripts in individual species (24, 25, 27, 28), this study focuses primarily on its interactions with RNA substrates.

In this work, we confirm that YhaM is a virulence factor and determine electron cryomicroscopy (cryo-EM) structures of *S. aureus* YhaM bound to two structurally distinct RNA targets. We show that YhaM forms a trimer of dimers with six YhaM protomers in total, organized in a ring-shaped structure. The N terminus adopts an oligonucleotide/oligosaccharide-binding fold (OB) domain that is the first point of contact with RNA and guides the 3'-end into the interior active site consisting of a histidine/aspartate-rich (HD) domain. In the structure of YhaM bound to the 3' end of its endogenous target *hpf* mRNA, at least two OB domains cooperate to bind the structured RNA substrate, with a third OB domain assisting by binding near the hairpin loop. In the context of ssRNA, one or two OB domains interact with the RNA to position its 3' end at its active site where exonucleolytic cleavage occurs. Two RNAs are engaged on each side of the ring and a barrier formed by YhaM prevents the 3'-ends from traversing the other side of the ring in contrast to other bacterial ribonucleases. These studies of YhaM provide insight into its mechanism of action, found to be important in *S. aureus* RNA metabolism.

Results

***S. aureus* YhaM Is Required for Full Virulence in a Galleria Model of Infection.** The impact of *S. aureus* YhaM in pathophysiology and global RNA regulation has not been defined. We used *Galleria mellonella* (greater wax moth) as a bacteremia model to quantify *S. aureus* virulence, based on extensive evidence demonstrating a positive correlation between staphylococcal virulence in *Galleria* and in mice (29–32). We first optimized larval size and inoculum dosage to 200 to 220 mg/caterpillar and 2.5 × 10^6 CFU/mL, respectively. When administered to *Galleria* larvae, the parental WT strain and the YhaM-complemented strain exhibited more rapid killing compared with the *S. aureus* Δ*yhaM* strain. We measured the time required to kill 50% of the caterpillars (LT_{50}) and found that the WT strain had an LT_{50} of 1.5 d, whereas the Δ*yhaM* knockout strain had an LT_{50} of 4 d. The attenuated virulence of the Δ*yhaM* knockout was fully rescued by chromosomally encoded-YhaM under the control of its native promoter (LT_{50} = 1.5 d) (Fig. 1). Consistent with our findings, an *S. aureus* Δ*yhaM* mutant is defective in macrophage invasion and intracellular survival (33), a phenotype likely attributable to disruption of mRNA turnover and/or DNA homeostasis during infection.

***S. aureus* YhaM Forms a Homohexameric Ring Structure as a Trimer of Dimers.** To investigate the role of YhaM, we used cryo-EM to determine the structure of the catalytically inactive YhaM D193A variant in complex with the 3' end of its endogenous *hpf* mRNA target to an overall resolution of 3.3 Å (Fig. 2 and *SI Appendix*, Fig. S1 and Table S1; this 40 nucleotide RNA will be referred to as *hpf* mRNA). Residue D193 is invariant among YhaM homologs and participates in metal ion coordination at the active site. Substitution of D193 with alanine yields a catalytically dead enzyme (16). A single YhaM protomer is 313 amino acids in length and forms a dimer with each protomer active site containing a PO_4^{3-} and two Mg^{2+} ions (Fig. 2*A* and *SI Appendix*, Fig. S2*A* and S3). The two protomers of each dimer are oriented in opposite directions relative to one another, leading their active sites to be accessible from opposite sides of the complex. Three YhaM dimers form a hexamer with individual protomers consisting of an N-terminal OB domain composed of a five-stranded β-barrel with two RNA-binding loops and a C-terminal α-helical HD domain (Fig. 2*A* and *SI Appendix*, Fig. S2*A*). YhaM protomers arrange in a ring-shaped trimer of dimers, with the catalytic HD domain containing the oligomerization interfaces (Fig. 2*B* and *SI Appendix*, Fig. S4). The hexameric assembly was previously validated by in vivo crosslinking in *S. aureus* (16) and supported by a recent *apo* structure of wild type *B. subtilis* YhaM (PDB code 9H3F) (20). This *apo* structure exhibits high structural similarity to our substrate-bound structure both in the overall HD domain conformation (1.1 Å C_α RMSD) and at the active site (0.8 Å C_α RMSD for active site residues H162, H192, A193, H217, H249, H250, and D273), indicating that the inactivating D193A mutation does not substantially alter the YhaM structure. Notably, the prior *B. subtilis* YhaM structure lacks well-resolved OB domains, likely due to the absence of a bound substrate. YhaM dimerization is facilitated primarily by hydrophobic interactions formed between two pairs of antiparallel α-helices (amino acids 158 to 176 and 264 to 288) and from C-terminal loops which wrap over the adjacent protomer of the same dimer and are anchored in place by hydrogen bonds (*SI Appendix*, Fig. S4 *A–D*). YhaM dimers oligomerize into a complete hexamer along an interface opposite to the dimerization interface through hydrophobic and electrostatic interactions between parallel α-helices spanning residues 214 to 247 (*SI Appendix*, Fig. S4 *E* and *F*). Together, these interactions facilitate oligomerization of YhaM into complete, functional hexamers with three accessible active sites per side of the ring.

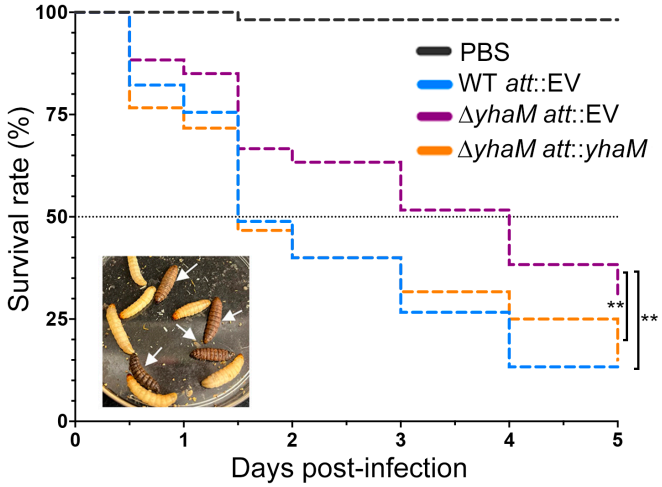

Fig. 1. The Δ*yhaM* null mutant is attenuated in virulence. Kaplan–Meier survival curves of *G. mellonella* larvae infected with *S. aureus* strains expressing single-copy YhaM. Except for the WT *att*::EV strain (n = 15 larvae per group per experiment), all other strains had n = 20 larvae per group per experiment, for a total of 60 larvae across three biological replicates. Survival differences were analyzed using the log-rank test, $^{**}P < 0.01$. Death was defined as absence of movement and complete melanization (see *Inset*). EV, empty integrative vector. PBS, phosphate buffer saline (negative control).

YhaM Recognizes *hpf* mRNA Using Multiple OB Domains. It was previously hypothesized that YhaM recognizes transcripts containing intrinsic terminator hairpins (24). The *hpf* mRNA possesses a predicted transcription terminator hairpin at its 3'-end, and YhaM is involved in recognition of this mRNA in vivo,

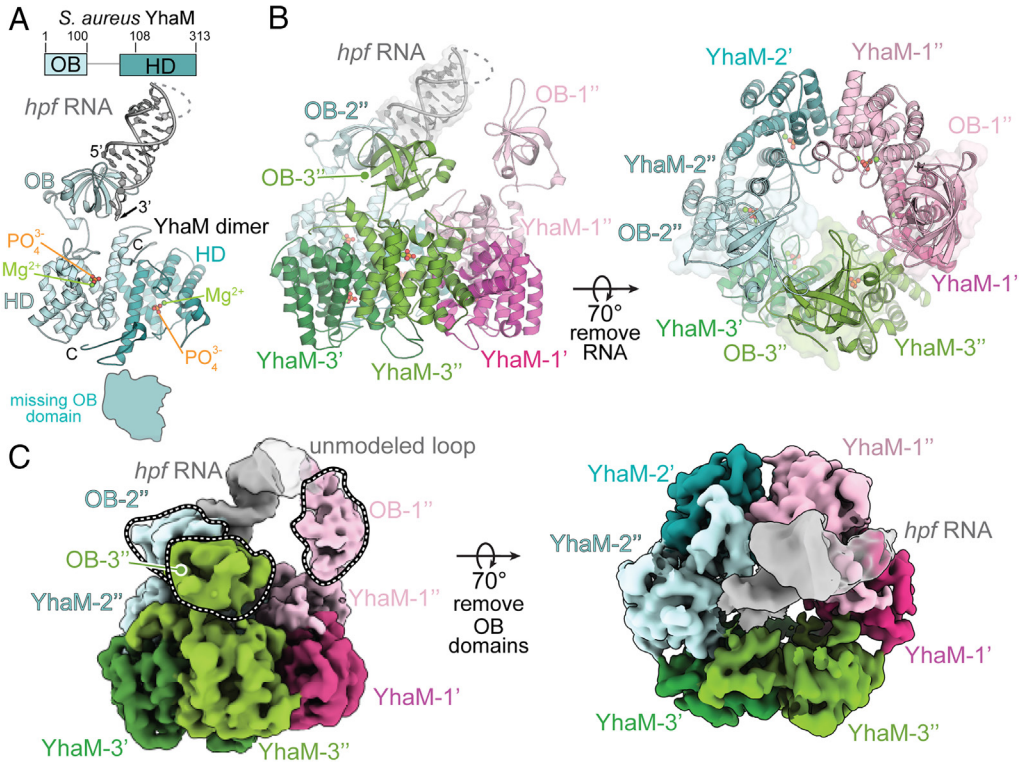

Fig. 2. YhaM forms a ring-shaped hexamer with three OB domains at each periphery. (*A*) Domain organization of a single YhaM dimer that directly contacts the *hpf* mRNA. The Mg^{2+} and PO_4^{3-} ions are shown as spheres in the YhaM active sites. This YhaM dimer has one OB domain that contacts the *hpf* mRNA while the other OB domain is likely dynamic in the absence of RNA bound to the opposite side of the YhaM ring. (*B*) Model of the YhaM hexamer bound to *hpf* mRNA (shown in gray surface). Dimerized YhaM pairs are depicted in similar colors. Three OB domains contact the RNA (*Left*). The loop region of *hpf* mRNA does not contain sufficient map quality to allow model building and is shown as a dotted line. Rotation of YhaM by ~70° horizontally with the removal of the *hpf* mRNA with the three OB domains (shown as surfaces on the other side of the YhaM ring; *Right*). (*C*) 3.3 Å map of the YhaM complex with the three OB domains outlined (*Left*). A ~70° horizontally rotated map with OB domains hidden shows the path of the *hpf* mRNA hairpin along the YhaM ring axis (*Right*).

resulting in trimming of 1 nucleotide from the 3'-end (16). We used a 40-nucleotide RNA containing the *hpf* terminator hairpin to investigate the interactions between catalytically inactive YhaM D193A and mRNA (*SI Appendix*, Table S1). In the resulting structure, either two or three OB domains are visible and interact with the *hpf* mRNA (3.3 Å and 3.5 Å resolution, respectively) (Fig. 2*B* and *SI Appendix*, Fig. S1). These N-terminal OB domains lie above the ring plane and interact with a single *hpf* mRNA substrate with OB-2" and OB-3" domains contacting the dsRNA stem and OB-1" engaging the hairpin loop (Fig. 2 *B* and *C*). Despite the presence of multiple RNA-binding OB domains and three active sites potentially accessible on each side of the ring, we observe density for only a single *hpf* RNA substrate on one side of the hexameric ring (Fig. 2). In an attempt to observe *hpf* RNA substrates on both sides of the ring, we increased the RNA concentration relative to YhaM but this complex was significantly aggregated on grids and thus we were unable to determine this structure.

Each N-terminal OB domain consists of a five-stranded β-barrel with two loops (loops L1 and L3) between β1-β2 and β4-β5 that directly interact with the phosphate backbone and form stacking interactions with the nucleotide immediately 5' of the hairpin (Fig. 3 *A* and *B*). The OB-2" and OB-3" domains closest to the ring engage both the 5'- and 3'-ends of the *hpf* mRNA (Fig. 3 *A–C* and *SI Appendix*, Figs. S2 and S3). The RNA-binding loops L1 and L3 of OB-2" and OB-3", respectively bind opposite sides

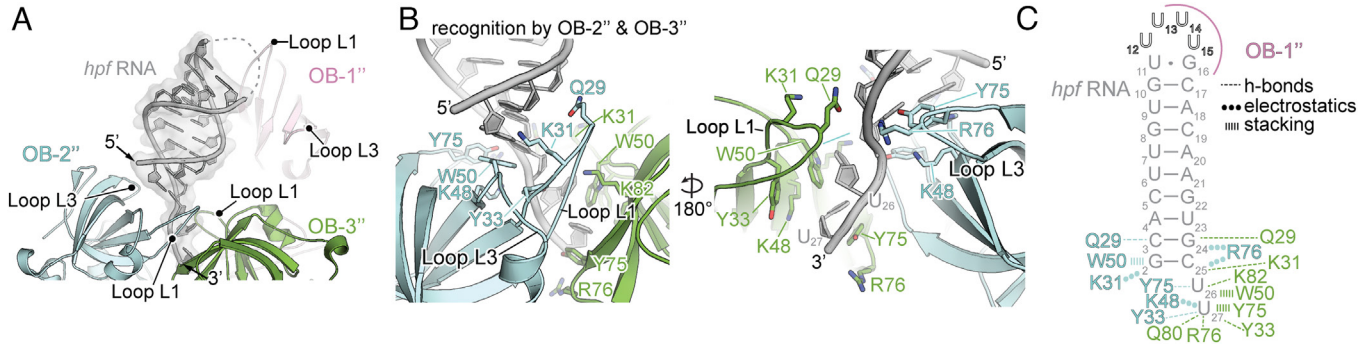

Fig. 3. Interactions of the *hpf* mRNA hairpin with three OB domains of YhaM. (*A*) Surface representation of the interactions of the three OB domains and the RNA-binding loops with the *yhaM* mRNA. (*B*) YhaM residues of OB-2″ and OB-3″ that interact with *hpf* mRNA, with specific interactions depicted in with a 180° rotation. (*C*) Schematic representation of the YhaM residues that interact with the *hpf* hairpin.

of the dsRNA, forming alternative interactions with the backbone (Fig. 3 *B* and *C*). In the OB-2" domain, loop L1 packs against the 5'-minor groove, residues Q29 and K31 interact with the RNA backbone, loop L3 residues Y75 and R76 form electrostatic and hydrogen bonds with the backbone of the opposite strand of the dsRNA, and W50 stacks with the 5' G_2 nucleobase (Fig. 3 *B* and *C*). G_2 is the first nucleotide modeled in the maps with the four nucleotides preceding not visible (*SI Appendix*, Table S1). On the opposite 3' side, three nucleotides are seen 3' of the stem of the hairpin (C_{25}, U_{26}, and U_{27}). The 3' terminus of the RNA substrate is disordered as it passes below the OB domains, suggesting there is slack between the 3' end and the nucleotides interacting with the OB domains that permit flexibility in the RNA. In this way, YhaM binds the base of its hairpin substrate while appearing to permit the 3' end of the substrate to hang loosely. At this 3' end, OB-3" residues Y33, Q80, and R76 form hydrogen bonds with the RNA backbone and Y75 stacks with the U_{27} nucleobase (Fig. 3 *B* and *C*). OB-3" residue W50 stacks with U_{26} and residues Q29 and K82 further engage the RNA. Therefore, the same OB-2" and OB-3" residues form interactions with the RNA, while OB-1" is the closest OB domain to the *yhaM* hairpin (Fig. 3*A* and *SI Appendix*, Fig. S3*A*. Loops L1 and L3 of OB-1" are positioned for interaction with the hairpin but are too distant for hydrogen bonding or electrostatic interactions to be assigned in our structure (Fig. 3 *A* and *C*). Further, the map quality for the RNA loop is not sufficient for modeling. However, there is a complementary electrostatic surface between the loop and OB-1", suggesting that these regions may be involved in binding (*SI Appendix*, Fig. S2*B*). This additional interaction could enhance YhaM binding to substrates containing a hairpin of a sufficient length near its 3' end that permits interactions with the third OB domain, providing a rationale for past observations that YhaM preferentially processes the hairpin-containing *hpf* mRNA (16).

In addition to particles displaying three well-resolved OB domains, we also observe a class of particles containing two well-resolved OB domains, corresponding to domains OB-2" and OB-3" (*SI Appendix*, Fig. S5). Relative to the three-OB structure, the *hpf* mRNA is positioned more orthogonal to the ring plane and is displaced away from the location of interaction with OB-1". OB-1" may serve a role in further increasing YhaM's affinity for substrates with RNA structural features of a preferred length and size, rather than serving as a necessary condition for substrate binding.

To assess the contribution of the OB domain, we generated an N-terminal truncation mutant lacking the first 80 amino acids ($YhaM^{\Delta OB}$). The recombinant $YhaM^{\Delta OB}$ protein assembles as a hexamer and retains the ability to cleave ssRNA and the *hpf* hairpin substrate, albeit with reduced efficiency compared to WT YhaM ($YhaM^{WT}$) (*SI Appendix*, Fig. S6). Notably, substitutions of the conserved W51 and Y76 residues within the OB domain of *B. subtilis* YhaM also do not substantially impair RNA cleavage (20). These results support the notion that the OB domain is not required for catalytic activity but instead facilitates substrate binding and/or optimal positioning.

Recognition of ssRNA for Exonuclease Activity by YhaM. Each YhaM dimer contains two active sites, with a total of six active sites in the YhaM hexameric complex and three active sites accessible from each side of the hexameric ring (Fig. 2). The HD domain active site contains histidine and aspartate residues (H162, H192, H217, H249, H250, D273) which coordinate divalent cations, with a preference for Mn^{2+} (16). In the YhaM structure bound to the *hpf* mRNA, the 3' end of the mRNA is mobile and density for its interaction with the active site of the HD domain is not observed. To understand how the active site of YhaM interacts with an RNA substrate, we next determined a structure of the YhaM D193A variant in complex with ssRNA to an overall resolution of 3.3 Å (refined without imposing symmetry) and 2.4 Å (refined with D3 symmetry for higher resolution of active site components; RNA not resolved) (Fig. 4 and *SI Appendix*, Figs. S7 and S8 and Table S3). Since the ssRNA substrate was based on a native substrate of *S. pyogenes* YhaM and was previously used to assess YhaM in vitro degradation activity (16), we reasoned that it may allow us to trap the 3' end of the RNA in the YhaM active site. There is a high degree of heterogeneity in our cryo-EM dataset, with particle subsets displaying different numbers and arrangements of well-resolved N-terminal OB domains on each side of the hexameric ring and with some protomers lacking visible OB domains (*SI Appendix*, Fig. S7). Particles with one, two, or three OB domains on each side of the ring are observed during 3D classification. However, very few particles contained all three OB domains, limiting the resolution of this complex (*SI Appendix*, Fig. S7). We next used 3D classification to select particles with two well-defined OB domains on each side of the ring. This classification shows two OB domains above (OB-3" and OB-2") and below (OB-1' and OB-2') the plane of the hexameric ring and each OB pair interacts with a ssRNA substrate (Fig. 4 *A* and *B* and *SI Appendix*, Fig. S8). Therefore, we see a total of two ssRNA molecules bound to YhaM despite the presence of six potential active sites.

To further ensure trapping of the ssRNA substrate at the active site, we used a buffer containing Mg^{2+} as the only divalent cation, as YhaM does not degrade RNA under these conditions (16). In our structure, we observe two Mg^{2+} ions at each of six YhaM active sites: one Mg^{2+} ion coordinated by H162, H192, and D273, and another coordinated by H217, H249, and H250 (Fig. 5). We observe density corresponding to a phosphate ion located between the two metal-binding centers, with residue K196 coordinating alongside the two active site Mg^{2+} ions (Fig. 5*B*). We propose that K196 may assist in coordinating the phosphate backbone of the substrate in the context of enzymatically active YhaM. The presence of a lysine residue at this position appears uncommon in other ribonucleases but can be found in other HD domain-containing structures, e.g., the *Persephonella marina* c-di-GMP phosphodiesterase PmGH (34) (PDB code 4MDZ).

In the YhaM-ssRNA structure, two YhaM N-terminal OB domains and a single catalytic HD domain on each side of the ring interact with the RNA substrate (Fig. 4*B*). A single YhaM protomer engages both the 5'-end of the RNA via its OB domain and the 3' end with its HD domain. Loops L1 and L3 of the N-terminal OB domain directly interact with the phosphate backbone and form stacking interactions with the 5'-end of the RNA similar to how YhaM interacts with *hpf* mRNA (Fig. 4 *C* and *D*). The two OB domains on each side of the ring engage the 5' end of a single RNA molecule, for example, OB-2" and OB-3" on one side and OB-1' and OB-2' on the other side (Fig. 4*A*). Together, the RNA-binding loops of each OB domain bind opposite sides of the RNA, forming alternative interactions with the backbone. At the 5' end of the RNA, YhaM residue W50 stacks with the first resolved RNA nucleotide, and residues Y75 and R76 in loop L3 of OB-3" (or OB-2') form electrostatic and hydrogen bonding interactions with the phosphate backbone of the first two well-resolved nucleotides (Fig. 4*D*). Loop 1 residues Q29 and K31 of OB-3" may additionally engage the 5' end of the RNA, but hydrogen bonds could not be confidently assigned for either RNA substrate. The backbone of the second and the third RNA nucleotides is further engaged by loop 1 residue Q29 in the OB-2" domain (or OB-1') (Fig. 4*D*). After the third nucleotide, the RNA

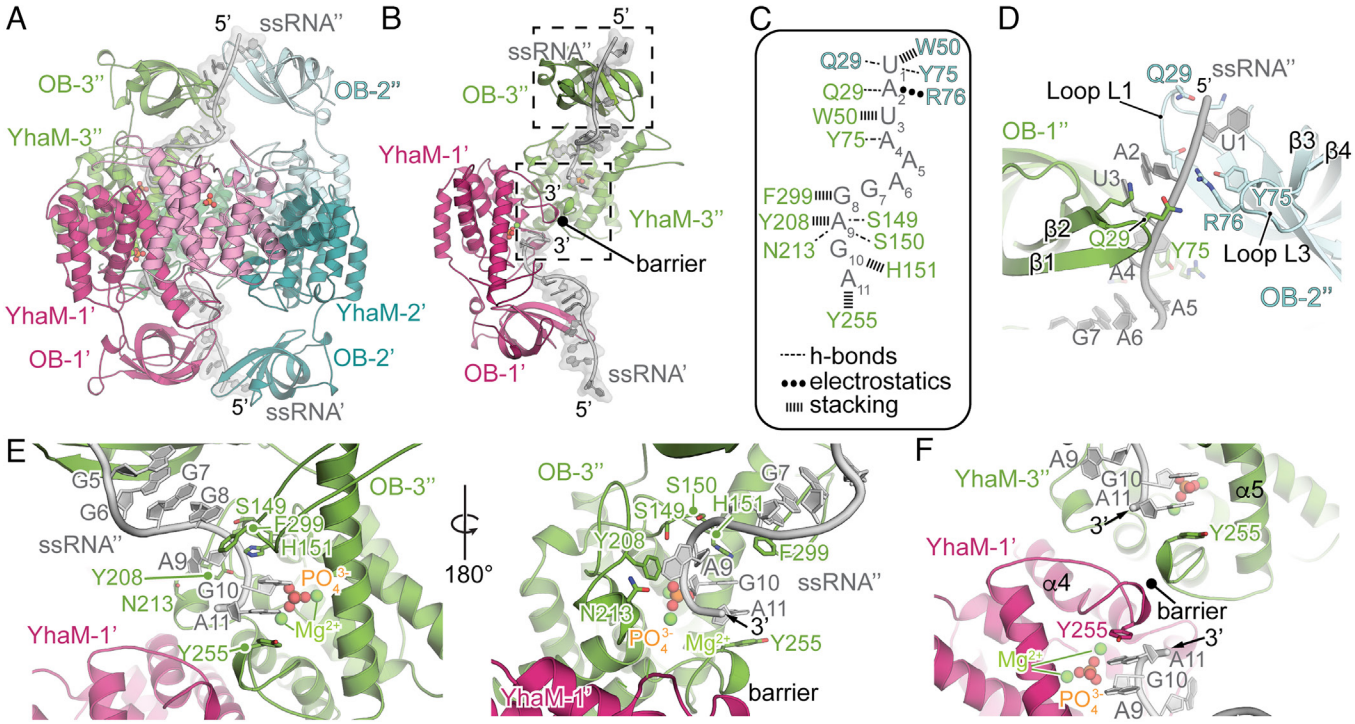

Fig. 4. Structure of YhaM bound to ssRNA. (*A*) Overview of YhaM bound to ssRNA. Each OB domain on each side of the ring interacts with RNA (in gray). The 3′ ends of the RNA are oriented inside the ring with the 5′ ends interacting with the OB domains. (*B*) Cut away presentation focusing on how YhaM-3″ (green) dimer engages both the 5′ and the 3′ ends of the ssRNA substrate. A barrier forms between YhaM-3″ (green) and YhaM-1″ (magenta) to prevent the 3′ ends of the RNA from interacting with each other. (*C*) YhaM residues of OB-3″ (green) and OB-2″ (blue) that interact with the 3′ end of the ssRNA. (*D*) Enlarged view showing how both OB-1′ and OB-2″ domains interact with the RNA upstream of the 3′ end, with the OB′ domain loops L1 and L3 engaging the RNA on both sides. (*E*) Enlarged view showing the interactions between YhaM and the 3′ end of the RNA (*Left*). Interactions of the 3′ end of RNA with YhaM aromatic amino acids showing a continuous stack that forms (RNA nucleotides G7 and G8 with F299 and H151, and G10, A11 with Y255) and specific interactions (G8 and A9 with S149 and S150; A9 with N213 and Y208) (*Right*). (*F*) YhaM residue Y255 interacts with the 3′ terminal A11 and serves as a barrier between the 3′ end of the other RNA molecule bound to YhaM-1′.

changes its trajectory, and Loop 3 residue Y75 of OB 2″ (or OB-1′) is positioned to stack with the nucleobase of RNA nucleotide 4 (Fig. 4*D*). Loop 3 residue R76 may also be positioned to participate in RNA binding but could not be confidently assigned to specific interactions in our structure. The 3′ end of the substrate RNA is held in place as it moves toward the active site by interactions with a groove on the interior face of the YhaM HD domain (Fig. 4*E*). This groove is lined with aromatic and polar amino acids which form stacking interactions with the RNA nucleobases and hydrogen bonds with the phosphate backbone. Amino acids Y255 and Y208 stack with the 3′ terminal and third-to-last nucleotides, respectively, while F299 stacks with the fourth-to-last nucleotide as it enters the interior-facing surface of YhaM (Fig. 4 *E* and *F*).

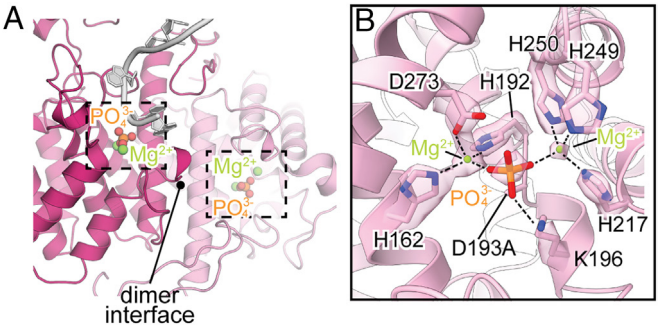

Fig. 5. YhaM active site. (*A*) The YhaM dimer interface and two HD active sites are boxed. (*B*) The HD active site shown with conserved His and Asp residues surrounding two Mg^{2+} ions and a phosphate. We used a YhaM D193A variant that is defective in mRNA cleavage.

Together, these interactions position the penultimate nucleotide at the active site, where it can undergo phosphohydrolysis, releasing the 3′ terminal nucleotide.

YhaM appears to process two ssRNA substrates simultaneously, with the 3′-ends of both RNAs positioned in adjacent YhaM active sites belonging to two different YhaM dimers (Fig. 4*B*). Stacking interactions with Y255 in each YhaM promoter both stabilize the 3′ nucleotide for phosphohydrolysis and appear to restrict each 3′-end of the RNA from further penetrating into the other side of the ring by a barrier formed by a loop between α4 and α5 (α4/α5 loop) (Fig. 4*B*). In addition to preventing the RNA substrates from penetrating deeper into the ring, the α4/α5 loop positions the 3′-end of the RNA at the active sites to allow each YhaM protomer to process its substrate.

Discussion

In this study, we determine that YhaM adopts a hexameric, ring-like structure capped with OB domains that interact with bound RNA substrates. All three YhaM dimers comprising the ring participate in RNA binding, RNA processing, or both. Interestingly, in this configuration, the two YhaM dimers containing the RNA-processing protomers each use their second protomer only as a structural component of the hexameric ring, neither binding nor processing RNA. The third YhaM dimer, which lies across the ring from the two RNA-processing protomers, exclusively participates in RNA binding, using its OB domains to bind the substrates immediately 5′ of the region bound by the OB domains of the RNA-processing protomers. The preference of YhaM particles for this orientation suggests that RNA binding by one side of the ring

may lead to conformational changes in the hexameric complex which lead to this configuration being preferred for binding of a second RNA molecule.

A notable difference we observe between our ssRNA-bound and dsRNA-bound structures is the presence of a second ssRNA molecule bound on the opposite side of the ring. We anticipate that this results from the preparation conditions of our cryo-EM samples, rather than representing distinct features of ssRNA and dsRNA handling by YhaM. Our ssRNA-containing sample was prepared with a higher molar concentration of RNA (12:1 relative to YhaM hexamers vs. 2:1 relative to YhaM hexamers). This was due to the observance of visible aggregates in micrographs of dsRNA-containing samples prepared at higher RNA concentrations. We do not observe features of the dsRNA-bound complex which would likely preclude independent binding of a second RNA molecule on the opposite side of the ring and propose that, like in the ssRNA-bound complex, it is likely competent for binding of a second substrate molecule.

Prior observation of YhaM's preference for mRNA containing the *hpf* transcription terminator hairpin is notable, as our structures indicate that neither the YhaM HD domain nor the OB domain directly inspect the Watson–Crick faces of substrate nucleobases, suggesting that YhaM lacks a mechanism to select substrates based on sequence. We therefore propose that in vivo YhaM selects RNAs for nucleolytic cleavage primarily based upon tertiary structure. We observe that the RNA density for dsRNA below the OB domains and at the YhaM active site is substantially weaker than for ssRNA in our cryo-EM datasets. One reason for this may be that YhaM preferentially binds the base of the *hpf* terminator hairpin via its OB domains rather than directly binding the RNA 3' end, leaving slack in the RNA as seen in our two structures. In contrast, in the absence of structured RNA to which YhaM would prefer to bind, YhaM may instead bind the 3' end directly, minimizing slack between the enzyme's active site and the OB domains. Notably, the YhaM OB domain does not appear to be required for RNA degradation or hexamerization, but a YhaM$^{\Delta OB}$ mutant exhibits a modest deficiency in ssRNA and *hpf* mRNA degradation activity in vitro, suggesting that the OB domain likely plays a role in substrate engagement and/or positioning which enhances its RNA degradation activity. The preference of YhaM for structured RNA elements could also provide a rationale for the previously observed low processivity of YhaM (24–26). Because YhaM lacks dedicated helicase domains, YhaM may struggle to unfold structured elements, limiting its ability to degrade dsRNAs. While YhaM has been observed to partially degrade RNA hairpins (16, 18), it may be difficult for YhaM to re-engage substrates in a crowded cellular environment, manifesting in the observed in vivo 3'-end trimming behavior rather than complete substrate degradation.

An outstanding question following our structural studies is whether the specificity of YhaM for hairpin-containing RNA substrates is affected by the lengths of the stem and loop. We observe in our cryo-EM data that while two YhaM OB domains coordinate to bind the base of the *hpf* mRNA hairpin, a third OB domain can approach the loop in a pose suggestive of interaction. The YhaM OB domain is connected to the catalytic HD domain through a short linker, which may permit flexibility in binding substrates of different hairpin and loop lengths. Consistent with this, 75 intrinsic terminator hairpin-containing RNAs targeted by *B. subtilis* YhaM contain loops ranging from 4 to 11 nucleotides (24).

A cryo-EM structure of wild type *B. subtilis* YhaM lacking nucleic acid molecules was recently published, permitting comparison with our structures of *S. aureus* YhaM D193A–RNA complexes (20). In other dinuclear and trinuclear HD domain phosphodiesterases, the aspartic acid of the HD motif (D193 in *S. aureus* YhaM) coordinates two metal ions at the active site (34–36) (Figs. 5 and 6). Substitution of this residue with alanine (as in D193A) abolishes enzyme activity, likely through increased interionic spacing due to the absence of coordination interactions with this residue. This would prevent polarization of a catalytic water molecule at the active site, preventing enzyme activity. Consistent with this, the spacing between Mg^{2+} ions in the WT structure is 5.2 Å, compared to 5.8 Å in our ssRNA-bound complex (Fig. 6 *C* and *D*). Interestingly, however, the interionic distance observed in the WT structure is still larger than is observed for active HD domain-containing enzymes (~3.4 Å to 3.7 Å, Fig. 6 *A* and *B*). It is possible that binding of a nucleic acid 3' end at the active site could induce formation of a "closed" conformation capable of phosphohydrolysis. Alternatively, the large interionic spacing at the active site could be a consequence of the divalent ion content of the sample buffers for both the WT and D193A structures. In both cases, samples were prepared in buffers containing magnesium as their sole divalent cations, in which YhaM is not competent for catalysis, instead preferring transition metal divalents such as Mn^{2+} or Co^{2+}. Mg^{2+} is less tolerant of coordination by soft Lewis bases such as the His residues present at the YhaM active site, which may preclude full metal ion occupancy at the active site and may consequently distort its structure.

The YhaM hexamer structurally resembles the phosphorolytic 3′-5′ exoribonuclease, PNPase. Both cleave ssRNA and ssDNA in vitro (16, 18, 37). PNPase forms a homotrimer consisting of three PNPase protomers and is a structural homolog of the eukaryotic RNA exosome (Fig. 7) (38–42). The N-terminal OB domain of YhaM forms a flexible, globular structure over the opening of the ring and contributes to RNA binding, much like the KH and S1 domains in PNPase. The KH domain of PNPase has been proposed to determine RNA directionality due to interactions between a loop in the KH domain (GSGG loop) and the backbone of the substrate RNA (39). It is possible the N-terminal OB-domains dictate RNA directionality through similar interactions. However, other features, such as the structure of the YhaM active site, may impact RNA directionality. Interestingly, PNPase is not essential for growth in Gram-positive bacteria but plays an important role in virulence, similar to what we observe for YhaM (43, 44). A critical difference between YhaM and PNPase is their enzymatic mechanisms. HD domain-containing enzymes like YhaM use hydrolytic mechanisms to process their substrates, using a water molecule activated by their coordinated metal ions. For YhaM, this would produce nucleoside monophosphates as products. On the other hand, PNPase uses a phosphorolytic mechanism, using inorganic phosphate ions to remove nucleotides from its substrates and producing nucleoside diphosphates as products. While we observe a phosphate ion bound at the YhaM active site, we propose that this does not reflect the enzymatic mechanism of YhaM and is instead present due to the use of phosphate in the buffer used to prepare cryo-EM samples. As an HD domain enzyme, YhaM uses a water molecule polarized by its active site divalent cations to perform hydrolysis (35). The phosphate ion observed at the active site occludes the space where the catalytic water would likely bind (e.g., as in PDB code 4MCW; Fig. 6) and competes with the phosphate group of the 3'-terminal nucleotide of the bound RNA, preventing observation of a state resembling the genuine catalytic arrangement of the active site.

Tunable gene expression is essential for cellular function and growth in bacteria, with RNases contributing by degrading mRNAs, rRNAs, and tRNAs. In *S. aureus*, YhaM reduces the stability of *hpf* mRNA (16), which encodes a hibernation factor that protects 30S ribosomal subunits from RNase R-mediated ribosome degradation

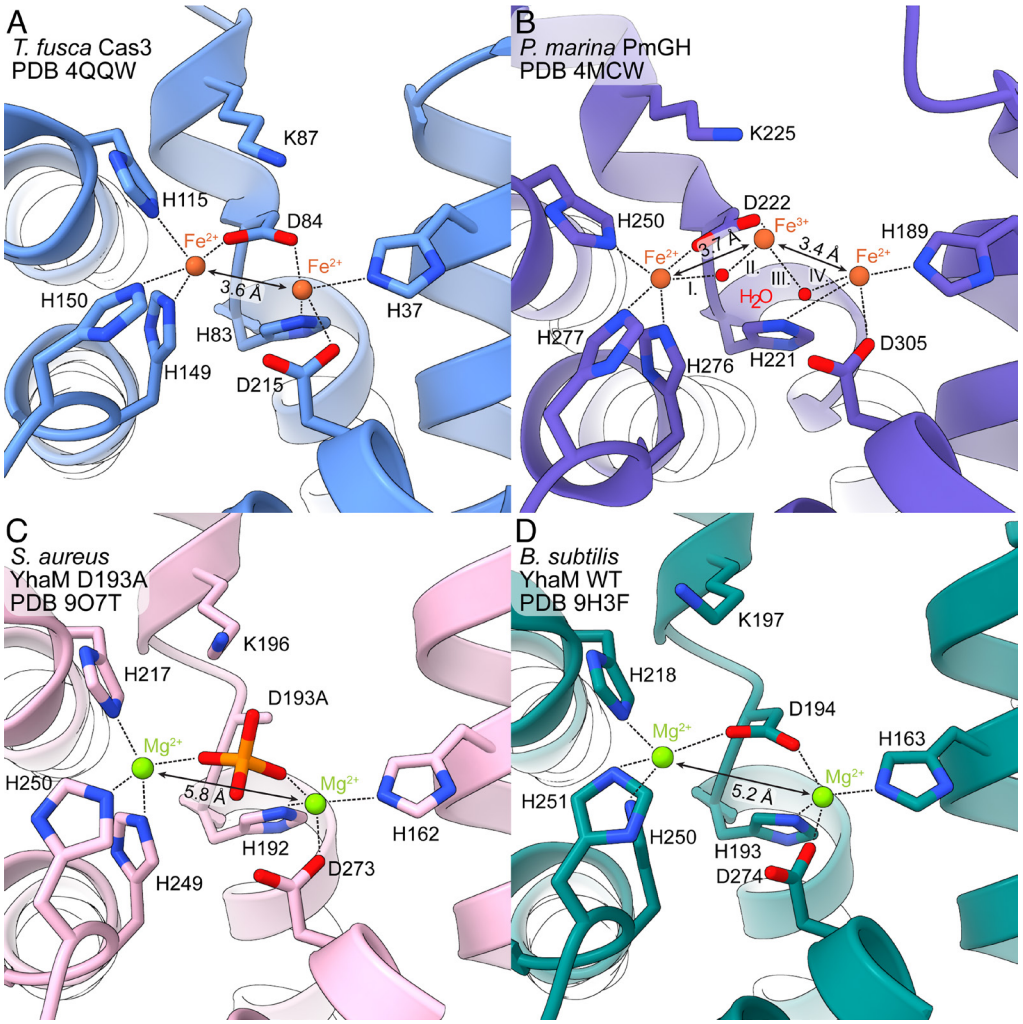

Fig. 6. HD domain phosphodiesterase active site architectures and interionic distances. (*A*) *Thermobifida fusca* Cas3 active site. (*B*) *P. marina* PmGH active site where the coordination bond lengths are as follows: I. 2.2 Å, II. 1.8 Å, III. 2.4 Å, and IV. 1.9 Å. (*C*) *S. aureus* YhaM D193A active site with bound phosphate ion. (*D*) *B. subtilis* WT YhaM active site.

(15, 16). Previous knockout studies have shown that only certain transcripts are stabilized in a Δ*yhaM* strain (24–26). The OB domain primarily interacts with the RNA backbone and does not directly inspect the Watson–Crick face of substrate nucleobases, therefore appearing to lack sequence specificity. It has been hypothesized that YhaM's specificity is determined by structural conformations of its RNA substrate, which could also impact processivity as YhaM does not exhibit helicase activity (24, 25). Since YhaM was originally identified as a DNA binding protein (21) that cleaves ssDNA but not dsDNA (20), perhaps one explanation for these data is that dsDNA cannot adopt conformations that dsRNA substrates adopt. A further consideration is that many YhaM processing sites in *S. pyogenes* and *B. subtilis* were identified close to Rho-independent transcriptional terminators and these data provide additional support for the recognition of RNA hairpins by YhaM (24, 26). YhaM has also been shown to cleave the *hpf* transcript following the hairpin loop of its intrinsic terminator, providing support for the role of YhaM in the recognition of structured RNAs like *hpf* (16).

Materials and Methods

Strains, Plasmids, and Oligos. All strains, oligos and plasmids are listed in *SI Appendix*, Tables S1 and S4. *S. aureus* USA300 JE2 is a community-associated methicillin-resistant *S. aureus* (CA-MRSA, GenBank CP000255). For single-copy chromosomal complementation of the Δ*yhaM* mutant, primers P2064 and P2065 were used to amplify a 1.25-kb *yhaM* region with its native promoter using pLI50P$_{yhaM}$-*yhaM* derivatives as template (16). The PCR product was digested with KpnI and BamHI and cloned into the same sites of pCL55. The pCL55 empty plasmid or its derivatives were propagated in *E. coli* DH10B, followed by electroporation to the Δ*yhaM* mutant or its parental JE2. The transformants were incubated at 30 °C on TSB agar plate supplemented with 7.5 μg/mL chloramphenicol for 36 to 48 h. Successful pCL55 integration to the *geh-att* site was confirmed by PCR using primers P2066/P2067, indicated by a 1.5-kb product spanning the *geh* flanking region. The expression of the chromosomal *yhaM* variants were confirmed by Western blots using anti-YhaM (1/4,000 dilution, protein A purified) (16).

***G. mellonella* Larvae Killing Assays.** Infectious studies were performed under the Arthropod Containment Level 2 (ACL-2) protocol BIO20240159 approved by the Northwestern University Institutional Biosafety Committee. We used established protocols tailored to the *S. aureus* infection model (29, 45). Briefly, *S. aureus* strains were subcultured in fresh 50 mL tryptic soy broth (TSB, no antibiotics) with initial OD_{600} of 0.05 and grown at 37 °C for ~4 h. Cells were harvested by centrifugation at 3,220 × g at 4 °C for 15 min. Pellets were washed with 10 mL sterile PBS, resuspended in 5 mL PBS and transferred to 15 mL TeenPrep tubes containing lysing Matrix B beads (MP Biomedicals). Cell aggregation was dispersed by vortexing for 30 s before serially diluting in 0.1 × PBS. Viable cell concentrations (in CFU) were measured on Bactobox (SBT Instruments) before administration. In parallel, bacterial inoculums were verified by standard dilution plating on TSB agar plates and CFU enumeration was performed after overnight incubation at 37 °C. To control batch-to-batch variations of *G. mellonella* larvae, all worms were purchased from Speedy Worm (Alexandria, MN), sorted by morphology (color,

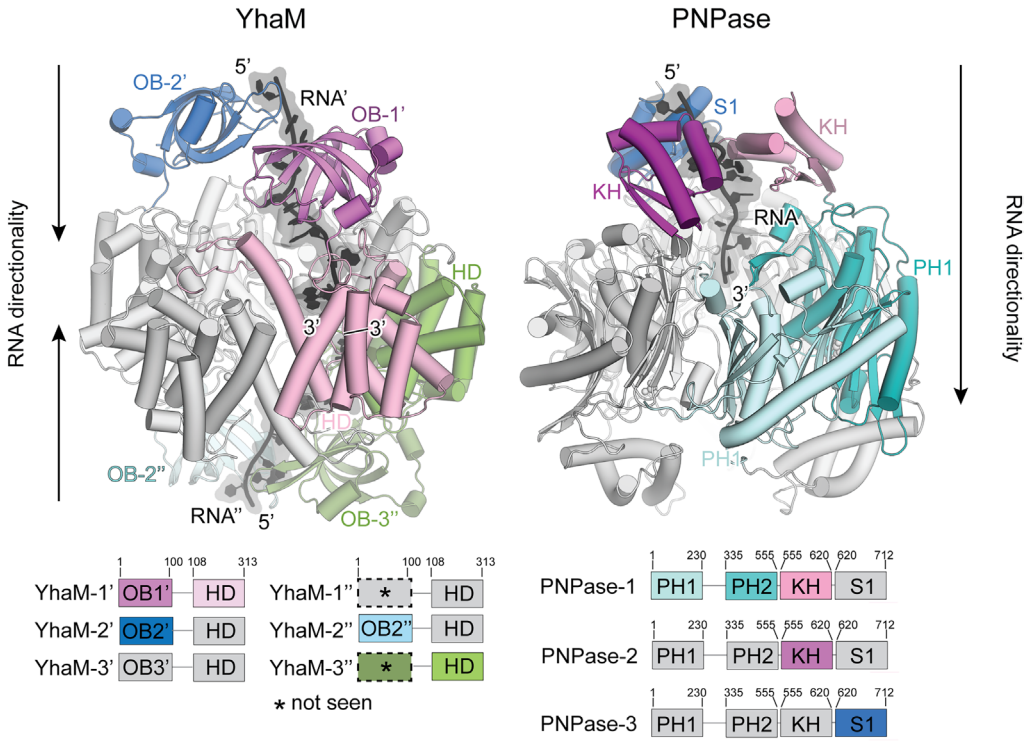

Fig. 7. Comparison of RNA-bound YhaM and PNPase. YhaM is a hexamer with OB domains that recognize ssRNA substrates on both sides of the ring (*Left*). The 5′ end of each RNA is bound to two OB domains and the 3′ end is guided to the catalytic HD domain (pink). Shown are the two HD domains that are positioned to perform catalysis and originate from two different YhaM dimers (YhaM-1′ and YhaM-3″). PNPase is a homotrimer that also forms a ring (*Right*; PDB code 4AM3). Two PH1 and PH2 catalytic domains are shown along with the RNA-binding domains (two KH domains and one S1 domain). The 3′ end of the RNA is guided to the two PH domains. One important difference between YhaM and PNPase is that PNPase processes the RNA in a unidirectional manner indicating that the RNA moves through the ring. In contrast, YhaM appears to be able to process two RNAs at a time but these RNAs do not pass through the ring because of the barrier formed by a loop between α4 and α5.

weight, and patterning), incubated at 16 °C incubator for 24 h, and a sample size of 15 to 20 per group per experiment was used. Ten microliters of 2.5 × 10^6 CFU *S. aureus* or sterile PBS were intrahemocoelically injected into the penultimate proleg of the larva using a calibrated syringe pump (KD Scientific Legato 100 Infuse) equipped with an EXEL 29.5-gauge 0.5 mL syringe (Fisher Scientific). The larvae were incubated at 37 °C for 5 d without food or water. Larvae mortality was scored every 12 h with the parameters that the larvae were both completely melanized and unresponsive to touch. Statistical analysis was performed using GraphPad Prism 10.1. and log-rank Mantel–Cox tests were used to compare survival curves.

YhaM Purification. *E. coli* BL21(DE3) transformed with plasmid for overexpressing catalytically inactive YhaM (pMCSG7-*yhaM*^{D193A}) (16) was grown in lysogeny broth (LB) supplemented with 100 μg mL^{-1} ampicillin until an optical density at 600 nm of 0.4. YhaM expression was induced with 0.5 mM isopropyl β-D1-thiogalactopyranoside (IPTG) for 3 h at 37 °C then cells were harvested by centrifugation. Cell pellet was resuspended in lysis buffer (50 mM NaH_2PO_4 pH 8.0, 300 mM NaCl, 10 mM imidazole, 5 mM β-mercaptoethanol, 0.1 mM phenylmethylsulfonyl fluoride, 0.5 mM benzamidine,) and lysed via three passages through an Emulsiflex. Filtered lysate was purified using affinity Ni^{2+}-NTA chromatography followed by anion exchange via DEAE Sepharose chromatography. Fractions containing YhaM were analyzed on 4 to 20% SDS-PAGE stained with Coomassie. Purified YhaM was concentrated to 1.1 mg/ml with a concentrator with a 30 kDa MWCO in a buffer 2 (50 mM NaH_2PO_4 pH 8.0, 150 mM NaCl, 20% glycerol, 7 mM $MgCl_2$, and 1 mM DTT), flash frozen in liquid nitrogen and stored at −80 °C.

Cryo-EM Sample Preparation, Data Collection, and Image Processing.
YhaM-hpf mRNA complex. Purified YhaM was exchanged into buffer 3 (50 mM NaH_2PO_4 pH 8.0, 150 mM NaCl, 1% glycerol, 7 mM $MgCl_2$). 40-mer RNA was purchased from IDT and resuspended in water (*SI Appendix*, Table S1). YhaM and RNA were complexed at a molar ratio of 2:1 of RNA to YhaM hexamer final YhaM concentration of 0.9 mg/mL for 5 min at 37 °C and incubated on ice before vitrification. C-Flat gold R1.2/1.3, 300 mesh holey carbon TEM grids (Electron Microscopy Sciences) were plasma cleaned for 15 s at 25 W forward power under a 75% argon, 25% oxygen atmosphere using a Gatan Solarus plasma cleaner. 3 μL of the YhaM–RNA complex was applied to grids, blotted for 5 s, and plunge-frozen in liquid ethane using a Vitrobot Mk IV (Thermo Fisher Scientific) at 4 °C and 100% humidity. Grids were stored in liquid nitrogen until data were collected.

15,724 micrographs were collected at the National Center for Cryo-EM Access and Training (NCCAT) using a TFS Krios 300 kV cryotransmission electron microscope (Thermo Fisher Scientific) operating at a nominal magnification of 165,000×. Movies were collected using a TFS Falcon 4i direct electron detector operating (calibrated pixel size of 0.7304 Å/px). Movies were collected with a dose rate of 8.83 $e^-/Å^2/s^{-1}$ for 6 s, yielding an accumulated dose of 53.0 $e^-/Å^2$. A nominal defocus range of 0.8 μm to 2.5 μm was used for image acquisition.

Prior to cryo-EM data processing, movie frames were aligned using Patch Motion Correction and contrast transfer function (CTF) parameters were estimated using Patch CTF Estimation in CryoSPARC 4.5.3 (46). Micrographs displaying poorer than 8 Å estimated resolution were discarded. Micrographs were denoised and the reference-free Blob Picker was used to pick particles from a subset of 2,354 micrographs, which were subsequently 2D classified, selected, and used to run 2D template-based particle picking on the entire dataset. Particles which were acquired from the carbon foil were discarded using a Micrograph Junk Detector job. 2,080,911 particle picks from 13,468 retained micrographs were extracted with a 2× binning factor (pixel size 1.46 Å/px) and downsampled box size of 128 pixels, then 2D classified with 200 classes. 736,114 particles were selected from 29 classes. Retained particles were passed into a Heterogeneous Refinement job using five ab initio reconstructions as initial volumes, resulting in two YhaM-like and three junk-like output volumes. YhaM-like classes were retained and used as inputs for two additional rounds of iterative Heterogeneous Refinement. 474,817 YhaM hexamer particles were selected, re-extracted at a pixel size of 0.73 Å/px and box size of 300, and subjected to Non-Uniform 3D Refinement, yielding an initial 3.8 Å reconstruction. Image shift data were used to split the dataset into optics groups, local and global CTF refinement were applied, and Reference Based Motion Correction was performed to yield a polished particle

set, with subsequent Non-Uniform Refinement yielding a 3.1 Å reconstruction. Particles were then subjected to 3D classification to resolve heterogeneity in particle N-terminal domain content, using 16 classes. 238,793 particles with density for 2 NTDs and 58,933 particles with 3 NTDs were selected. Particles containing 2 NTDs were reclassified with 16 classes to homogenize RNA content, yielding a final stack of 224,020 particles resulting in a 3.3 Å reconstruction after Non-Uniform Refinement. Particles containing 3 NTDs were reclassified with 4 classes to homogenize NTD content, yielding a final stack of 42,145 particles producing a 3.4 Å reconstruction from Non-Uniform Refinement.

YhaM-ssRNA complex. Purified YhaM was exchanged into buffer 3 (50 mM NaH_2PO_4 pH 8.0, 150 mM NaCl, 1% glycerol, 7 mM $MgCl_2$). 15-mer ssRNA was purchased from IDT and resuspended in water (*SI Appendix*, Table S1). YhaM and RNA were complexed at a molar ratio of 12:1 of RNA to YhaM hexamer (2:1 RNA to YhaM monomer) and final YhaM concentration of 1.1 mg/mL for 5 min at 37 °C and incubated on ice before vitrification. C-Flat gold R1.2/1.3, 300 mesh holey carbon TEM grids (Electron Microscopy Sciences) were plasma cleaned for 15 s at 25 W forward power under a 75% argon, 25% oxygen atmosphere using a Gatan Solarus plasma cleaner. 3 μL of the YhaM–RNA complex was applied to grids, blotted for 5.5 s, and plunge-frozen in liquid ethane using a Vitrobot Mk IV (Thermo Fisher Scientific) at 4 °C and 100% humidity. Grids were stored in liquid nitrogen until data were collected.

14,007 micrographs were collected at the National Center for Cryo-EM Access and Training (NCCAT) using a TFS Krios 300 kV cryotransmission electron microscope (Thermo Fisher Scientific) operating at a nominal magnification of 105,000×. Movies were collected using a Gatan K3 direct electron detector operating in superresolution mode (calibrated pixel size of 0.4124 Å/px). Movies were collected with a dose rate of 29.4 $e^-/Å^2/s^{-1}$ for 1.6 s, yielding an accumulated dose of 47.0 $e^-/Å^2$. Intermediate frames were recorded every 0.04 s, yielding a total of 40 frames per movie. A nominal defocus range of 0.5 μm to 2.0 μm was used for image acquisition.

Prior to cryo-EM data processing, movie frames were aligned using Patch Motion Correction and contrast transfer function (CTF) parameters were estimated using Patch CTF Estimation in CryoSPARC 4.5.3 (46). Micrographs displaying poorer than 5 Å estimated resolution were discarded. The reference-free Blob Picker was used to pick particles from a random subset of 250 micrographs, which were subsequently 2D classified, selected, and used to train a Topaz particle picking model for particle picking from the entire dataset. Micrographs which were acquired on the carbon foil were manually discarded using a Manually Curate Exposures job by identifying micrographs with anomalously high CTF fit resolutions and high background noise relative to their estimated defocus. 8,389,618 particle picks from 12,453 retained micrographs were extracted with a 4× binning factor (pixel size 1.65 Å/px) and downsampled box size of 128 pixels, then 2D classified with 100 classes. 4,364,915 particles were selected from 24 classes, then passed into a second round of 2D classification with 100 classes. 3,524,806 particles were selected from 48 classes. Retained particles were passed into a Heterogeneous Refinement job using two ab initio reconstructions generated from 200,000 particles as initial volumes: one volume corresponding to YhaM hexamer and one junk volume. 3,127,932 YhaM hexamer particles were selected, re-extracted at a pixel size of 0.825 Å/px and box size of 256, and subjected to homogeneous 3D refinement, yielding an initial 3.3 Å reconstruction. Image shift data were used to split the dataset into optics groups, local and global CTF refinement were applied, and Reference Based Motion Correction was performed to yield a polished particle set, with subsequent homogeneous 3D refinement yielding a 2.6 Å reconstruction. CTF-refined particles were subjected to homogeneous 3D refinement with imposed D3 symmetry, yielding a reconstruction of the hexameric ring of YhaM HD domains to an overall resolution of 2.4 Å. CTF-refined particles from the asymmetric 3D refinement were then subjected to 3D classification to resolve compositional heterogeneity in particle N-terminal domain content, using 50 classes per classification without a focus mask. Three classification jobs were performed, iteratively passing selected particles from one job to the next: First, 1,858,123 particles were selected containing at least two clearly defined N-terminal domains above the ring plane; second, 697,247 particles were selected which contained at least one clearly defined N-terminal domain below the ring plane; finally, 78,075 particles were selected containing exactly two clearly defined N-terminal domains on each side of the ring plane. These particles were subjected to homogeneous 3D refinement, yielding a final 3.3 Å reconstruction.

Cryo-EM Model Building and Refinement. The final 3D refinement maps from CryoSPARC were sharpened using the Autosharpen feature in PHENIX 1.21.2–5419 (ssRNA, C1 refinement map) or in CryoSPARC (ssRNA, D3 refinement map; dsRNA maps) (47). An initial molecular model of YhaM hexamers was automatically built into the sharpened map using ModelAngelo (48). Amino acids not built automatically were added to the model and fit into the sharpened map manually using COOT 0.9.6 (49). Models of the YhaM RNA substrate were built manually in COOT. To model NTDs not automatically built by ModelAngelo, copies of the YhaM NTD model were rigidly fit into the unsharpened 3D refinement map using PHENIX Real Space Refinement and combined with the YhaM hexamer model. Final flexible model refinement was performed using PHENIX Real Space Refinement, with clashes and Ramachandran outliers being fixed manually in COOT. Model validation was performed using MolProbity in PHENIX (50, 51).

Data, Materials, and Software Availability. Atomic coordinates and maps have been deposited [PDB codes 9O7T (52), 9OV1 (53), 9YPF (54), and 9YPE (55) and EMDB codes 70208 (56), 70886 (57), 73296 (58), and 73295 (59)].

ACKNOWLEDGMENTS. This work was supported by the NIH grants R01 GM121359 and R01 AI150986 (to M.-N.F.Y.), R01 GM093278 and R35 GM156629 (to C.M.D.), T32 GM008367 (to J.T. and J.M.M.), and an NSF GRFP fellowship 2021310209 (to J.T.). This study was also supported by the Robert P. Apkarian Integrated Electron Microscopy Core at Emory University, which is subsidized by the School of Medicine and Emory College of Arts and Sciences. Some of this work was performed at the National Center for CryoEM Access and Training and the Simons Electron Microscopy Center located at the New York Structural Biology Center, supported by the NIH Common Fund Transformative High Resolution Cryo-Electron Microscopy program (U24 GM129539 and NIGMS R24 GM154192) and by grants from the Simons Foundation (SF349247) and NY State Assembly.

1. B. Beckert *et al.*, Structure of the *Bacillus subtilis* hibernating 100S ribosome reveals the basis for 70S dimerization. *EMBO J.* **36**, 2061–2072 (2017).
2. T. Prossliner, K. Skovbo Winther, M. A. Sorensen, K. Gerdes, Ribosome hibernation. *Annu. Rev. Genet.* **52**, 321–348 (2018).
3. H. A. Feaga, M. Kopylov, J. K. Kim, M. Jovanovic, J. Dworkin, Ribosome dimerization protects the small subunit. *J. Bacteriol.* **202**, e00009-20 (2020).
4. T. Prossliner, K. Gerdes, M. A. Sorensen, K. S. Winther, Hibernation factors directly block ribonucleases from entering the ribosome in response to starvation. *Nucleic Acids Res.* **49**, 2226–2239 (2021).
5. S. Koli, S. Shetty, Ribosomal dormancy at the nexus of ribosome homeostasis and protein synthesis. *Bioessays* **46**, e2300247 (2024).
6. K. Helena-Bueno, L. I. Chan, S. V. Melnikov, Rippling life on a dormant planet: Hibernation of ribosomes, RNA polymerases, and other essential enzymes. *Front. Microbiol.* **15**, 1386179 (2024).
7. D. W. Gohara, M. F. Yap, Survival of the drowsiest: The hibernating 100S ribosome in bacterial stress management. *Curr. Genet.* **64**, 753–760 (2018).
8. A. Basu, M. N. Yap, Ribosome hibernation factor promotes Staphylococcal survival and differentially represses translation. *Nucleic Acids Res.* **44**, 4881–4893 (2016).
9. D. Matzov *et al.*, The cryo-EM structure of hibernating 100S ribosome dimer from pathogenic Staphylococcus aureus. *Nat. Commun.* **8**, 723 (2017).
10. I. Khusainov *et al.*, Structures and dynamics of hibernating ribosomes from *Staphylococcus aureus* mediated by intermolecular interactions of HPF. *EMBO J.* **36**, 2073–2087 (2017).
11. A. Basu, M. N. Yap, Disassembly of the *Staphylococcus aureus* hibernating 100S ribosome by an evolutionarily conserved GTPase. *Proc. Natl. Acad. Sci. U.S.A.* **114**, E8165–E8173 (2017).
12. A. Basu, K. E. Shields, C. S. Eickhoff, D. F. Hoft, M. N. Yap, Thermal and nutritional regulation of ribosome hibernation in *Staphylococcus aureus*. *J. Bacteriol.* **200**, e00426-18 (2018).
13. A. Basu, K. E. Shields, M. F. Yap, The hibernating 100S complex is a target of ribosome-recycling factor and elongation factor G in *Staphylococcus aureus*. *J. Biol. Chem.* **295**, 6053–6063 (2020).
14. A. Liponska, M. F. Yap, Hibernation-promoting factor sequesters *Staphylococcus aureus* ribosomes to antagonize RNase R-mediated nucleolytic degradation. *mBio* **12**, e0033421 (2021).
15. L. Dimitrova-Paternoga *et al.*, Structural basis of ribosomal 30S subunit degradation by RNase R. *Nature* **626**, 1133–1140 (2024).
16. A. Liponska, H. Lee, M. F. Yap, Staphylococcal exoribonuclease YhaM destabilizes ribosomes by targeting the mRNA of a hibernation factor. *Nucleic Acids Res.* **52**, 8998–9013 (2024).
17. C. Condon, J. Piton, F. Braun, Distribution of the ribosome associated endonuclease Rae1 and the potential role of conserved amino acids in codon recognition. *RNA Biol.* **15**, 683–688 (2018).
18. I. A. Oussenko, R. Sanchez, D. H. Bechhofer, *Bacillus subtilis* YhaM, a member of a new family of 3′-to-5′ exonucleases in gram-positive bacteria. *J. Bacteriol.* **184**, 6250–6259 (2002).
19. F. C. Walker, L. Chou-Zheng, J. A. Dunkle, A. Hatoum-Aslan, Molecular determinants for CRISPR RNA maturation in the Cas10-Csm complex and roles for non-Cas nucleases. *Nucleic Acids Res.* **45**, 2112–2123 (2017).

20. J. Hanssmann *et al.*, A conserved nuclease facilitates environmental DNA uptake. *Nucleic Acids Res.* **53**, gkaf443 (2025).
21. Q. Zhang, S. Soares de Oliveira, R. Colangeli, M. L. Gennaro, Binding of a novel host factor to the pT181 plasmid replication enhancer. *J. Bacteriol.* **179**, 684–688 (1997).
22. M. F. Noirot-Gros *et al.*, An expanded view of bacterial DNA replication.. *Proc. Natl. Acad. Sci. U.S.A.* **99**, 8342–8347 (2002).
23. L. Chou-Zheng, A. Hatoum-Aslan, Critical roles for "housekeeping" nucleases in type III CRISPR-Cas immunity. *eLife* **11**, e81897 (2022).
24. J. B. Lalanne *et al.*, Evolutionary convergence of pathway-specific enzyme expression stoichiometry. *Cell* **173**, 749–761.e738 (2018).
25. A. L. Lecrivain *et al.*, In vivo 3′-to-5′ exoribonuclease targetomes of *Streptococcus pyogenes*. *Proc. Natl. Acad. Sci. U.S.A.* **115**, 11814–11819 (2018).
26. L. Broglia *et al.*, An RNA-seq based comparative approach reveals the transcriptome-wide interplay between 3′-to-5′ exoRNases and RNase Y. *Nat. Commun.* **11**, 1587 (2020).
27. J. Hor *et al.*, Grad-seq in a Gram-positive bacterium reveals exonucleolytic sRNA activation in competence control. *EMBO J.* **39**, e103852 (2020).
28. S. Chhabra, Z. F. Mandell, B. Liu, P. Babitzke, D. H. Bechhofer, Analysis of mRNA decay intermediates in *Bacillus subtilis* 3′ exoribonuclease and RNA helicase mutant strains. *mBio* **13**, e0040022 (2022).
29. G. Menard *et al.*, Galleria mellonella larvae as an infection model to investigate sRNA-mediated pathogenesis in *Staphylococcus aureus*. *Front. Cell. Infect. Microbiol.* **11**, 631710 (2021).
30. P. Ebner *et al.*, Excreted cytoplasmic proteins contribute to pathogenicity in *Staphylococcus aureus*. *Infect. Immun.* **84**, 1672–1681 (2016).
31. Y. Lu *et al.*, Modulation of MRSA virulence gene expression by the wall teichoic acid enzyme TarO. *Nat. Commun.* **14**, 1594 (2023).
32. G. K. Mannala *et al.*, Whole-genome comparison of high and low virulent *Staphylococcus aureus* isolates inducing implant-associated bone infections. *Int. J. Med. Microbiol.* **308**, 505–513 (2018).
33. I. Rodrigues Lopes *et al.*, Systematic identification of bacterial factors driving *Staphylococcus aureus* intracellular lifestyle in non-professional phagocytes. *Nat. Commun.* **16**, 10907 (2025).
34. D. Bellini *et al.*, Crystal structure of an HD-GYP domain cyclic-di-GMP phosphodiesterase reveals an enzyme with a novel trinuclear catalytic iron centre. *Mol. Microbiol.* **91**, 26–38 (2014).
35. M. Langton *et al.*, The HD-Domain metalloprotein superfamily: An apparent common protein scaffold with diverse chemistries. *Catalysts* **10**, 1191 (2020).
36. Y. Huo *et al.*, Structures of CRISPR Cas3 offer mechanistic insights into Cascade-activated DNA unwinding and degradation. *Nat. Struct. Mol. Biol.* **21**, 771–777 (2014).
37. P. P. Cardenas *et al.*, Polynucleotide phosphorylase exonuclease and polymerase activities on single-stranded DNA ends are modulated by RecN, SsbA and RecA proteins. *Nucleic Acids Res.* **39**, 9250–9261 (2011).
38. S. Nurmohamed, B. Vaidialingam, A. J. Callaghan, B. F. Luisi, Crystal structure of *Escherichia coli* polynucleotide phosphorylase core bound to RNase E, RNA and manganese: Implications for catalytic mechanism and RNA degradosome assembly. *J. Mol. Biol.* **389**, 17–33 (2009).
39. S. W. Hardwick, T. Gubbey, I. Hug, U. Jenal, B. F. Luisi, Crystal structure of *Caulobacter crescentus* polynucleotide phosphorylase reveals a mechanism of RNA substrate channelling and RNA degradosome assembly. *Open Biol.* **2**, 120028 (2012).
40. C. L. Lin, Y. T. Wang, W. Z. Yang, Y. Y. Hsiao, H. S. Yuan, Crystal structure of human polynucleotide phosphorylase: Insights into its domain function in RNA binding and degradation. *Nucleic Acids Res.* **40**, 4146–4157 (2012).
41. T. Dendooven *et al.*, A cooperative PNPase-Hfq-RNA carrier complex facilitates bacterial riboregulation. *Mol. Cell* **81**, 2901–2913.e2905 (2021).
42. L. G. Miller *et al.*, Selective 8-oxo-rG stalling occurs in the catalytic core of polynucleotide phosphorylase (PNPase) during degradation. *Proc. Natl. Acad. Sci. U.S.A.* **121**, e2317865121 (2024).
43. M. O. Clements *et al.*, Polynucleotide phosphorylase is a global regulator of virulence and persistency in *Salmonella enterica*. *Proc. Natl. Acad. Sci. U.S.A.* **99**, 8784–8789 (2002).
44. J. A. Rosenzweig, A. K. Chopra, The exoribonuclease polynucleotide phosphorylase influences the virulence and stress responses of Yersiniae and many other pathogens. *Front. Cell. Infect. Microbiol.* **3**, 81 (2013).
45. P. J. Hesketh-Best, M. V. Mouritzen, K. Shandley-Edwards, R. A. Billington, M. Upton, *Galleria mellonella* larvae exhibit a weight-dependent lethal median dose when infected with methicillin-resistant *Staphylococcus aureus*. *Pathog. Dis.* **79**, ftab003 (2021).
46. A. Punjani, J. L. Rubinstein, D. J. Fleet, M. A. Brubaker, cryoSPARC: Algorithms for rapid unsupervised cryo-EM structure determination. *Nat. Methods* **14**, 290–296 (2017).
47. D. Liebschner *et al.*, Macromolecular structure determination using X-rays, neutrons and electrons: Recent developments in Phenix. *Acta Crystallogr. D Struct. Biol.* **75**, 861–877 (2019).
48. K. Jamali *et al.*, Automated model building and protein identification in cryo-EM maps. *Nature* **628**, 450–457 (2024).
49. P. Emsley, K. Cowtan, Coot: Model-building tools for molecular graphics. *Acta Crystallogr. D Biol. Crystallogr.* **60**, 2126–2132 (2004).
50. C. J. Williams *et al.*, MolProbity: More and better reference data for improved all-atom structure validation. *Protein Sci.* **27**, 293–315 (2018).
51. V. B. Chen *et al.*, MolProbity: All-atom structure validation for macromolecular crystallography. *Acta Crystallogr. D Biol. Crystallogr.* **66**, 12–21 (2010).
52. J. M. Mattingly, J. R. Tanquary, C. M. Dunham, S. aureus YhaM D193A, 4 N-terminal domains, 2 RNA substrates. Protein Data Bank. https://www.rcsb.org/structure/9O7T. Deposited April 15 2025.
53. J. M. Mattingly, J. R. Tanquary, C. M. Dunham, S. aureus YhaM D193A hexamer, D3 refinement. Protein Data Bank. https://www.rcsb.org/structure/9OV1. Deposited 29 May 2025.
54. J. M. Mattingly, J. R. Tanquary, C. M. Dunham, S. aureus YhaM D193A hexamer, 3 NTDs, hairpin RNA substrate. Protein Data Bank. https://www.rcsb.org/structure/9YPF. Deposited 14 October 2025.
55. J. M. Mattingly, J. R. Tanquary, C. M. Dunham, S. aureus YhaM D193A hexamer, 2 NTDs, hairpin RNA substrate. Protein Data Bank. https://www.rcsb.org/structure/9YPE. Deposited 14 October 2025.
56. J. M. Mattingly, J. R. Tanquary, C. M. Dunham, S. aureus YhaM D193A, 4 N-terminal domains, 2 RNA substrates. Electron Microscopy Data Bank. https://www.ebi.ac.uk/emdb/EMD-70208. Deposited 15 April 2025.
57. J. M. Mattingly, J. R. Tanquary, C. M. Dunham, S. aureus YhaM D193A hexamer, D3 refinement. Electron Microscopy Data Bank. https://www.ebi.ac.uk/emdb/EMD-70886. Deposited 29 May 2025.
58. J. M. Mattingly, J. R. Tanquary, C. M. Dunham, S. aureus YhaM D193A hexamer, 3 NTDs, hairpin RNA substrate. Electron Microscopy Data Bank. https://www.ebi.ac.uk/emdb/EMD-73296. Deposited 14 October 2025.
59. J. M. Mattingly, J. R. Tanquary, C. M. Dunham, S. aureus YhaM D193A hexamer, 2 NTDs, hairpin RNA substrate. Electron Microscopy Data Bank. https://www.ebi.ac.uk/emdb/EMD-73295. Deposited 14 October 2025.